



**HAL**  
open science

# Damping adjustment of a nonlinear vibration absorber using an electro-magnetomechanical coupling

Bastien Cadiou, Cyrille Stephan, Adrien Renoult, Guilhem Michon

► **To cite this version:**

Bastien Cadiou, Cyrille Stephan, Adrien Renoult, Guilhem Michon. Damping adjustment of a nonlinear vibration absorber using an electro-magnetomechanical coupling. *Journal of Sound and Vibration*, 2022, 518, pp.116508. 10.1016/j.jsv.2021.116508 . hal-03578845

**HAL Id: hal-03578845**

**<https://hal.science/hal-03578845>**

Submitted on 17 Feb 2022

**HAL** is a multi-disciplinary open access archive for the deposit and dissemination of scientific research documents, whether they are published or not. The documents may come from teaching and research institutions in France or abroad, or from public or private research centers.

L'archive ouverte pluridisciplinaire **HAL**, est destinée au dépôt et à la diffusion de documents scientifiques de niveau recherche, publiés ou non, émanant des établissements d'enseignement et de recherche français ou étrangers, des laboratoires publics ou privés.

# Damping adjustment of a nonlinear vibration absorber using an electro-magnetomechanical coupling

Bastien Cadiou<sup>a,1,\*</sup>, Cyrille Stephan<sup>a</sup>, Adrien Renoult<sup>a</sup>, Guilhem Michon<sup>b</sup>

<sup>a</sup>ONERA, 29 Avenue de la Division Leclerc, 92320, Chatillon, France

<sup>b</sup>Université de Toulouse, ICA, ISAE-SUPAERO, CNRS, 3 Rue Caroline Aigle, 31400, Toulouse, France

---

## Abstract

Vibration absorbers are known for their use in vibration mitigation. In particular, nonlinear vibration absorbers have been of great interest for vibratory level reduction as they do not have to be tuned to the natural frequency of their supporting structure. In order to obtain satisfactory operations of the absorber (energy necessary for its activation and dissipated vibratory level), it is necessary to identify the correct parameters of the absorber which are its nonlinear stiffness and damping. However, when moving from analytics to designing an experimental prototype, it is complicated to have the appropriate parameter values, especially damping, because it is very difficult (or even impossible) to adjust a precise value for a mechanical assembly. As a consequence, this bad adjustment leads to an inefficiency of the absorber and unsatisfactory results. To avoid this lack of robustness, the addition of a multiphysical coupling, to a nonlinear absorber is studied in this paper in order to create an equivalent damping coefficient from another nature : electro-magnetomechanical. This new damping generated is adapted and allows to adjust the equivalent damping coefficient of the absorber to get the best efficiency, analytically and experimentally.

*Keywords:* Vibrations, Control, Nonlinear Dynamics, Multiphysics

---

## 1. Introduction

Structures subjected to dynamic excitation may exhibit harmful vibrations, potentially reducing their lifespan. Therefore, vibration mitigation has received great interest [1]. Passive linear vibration absorbers, called TMDs (Tuned Mass Damper) are frequently used in industry to reduce vibration level of critical components. For a dynamic solicitation close to the natural frequency of the main structure to be damped, they are efficient for a mass ratio between the TMD and the modal mass of the structure of about 5-10%. However, the natural frequency of the TMD must be tuned to the structure otherwise a loss of efficiency appears quickly.

In the last decade, nonlinear vibration absorbers, usually known as Nonlinear Energy Sinks (NES), have been the object of numerous studies in the field of Nonlinear Dynamics to circumvent the limits of TMD. The substitution of the linear stiffness by an essentially nonlinear one allows the NES to not have a natural frequency and to adapt itself to the supporting structure, hence initiating the energy transfer for a mass ratio of about 1% only. Analytical models of the dynamical behavior of NES have shown a promising potential to dissipate energy. Experimental and theoretical studies have shown that the nonlinearity of the NES allows an irreversible transfer of energy, known as Targeted Energy Transfer, from the primary system to the NES [2–5]. Passive control of resonance using a NES was studied analytically [6, 7] and experimentally [8, 9]. Investigations on the control of aeroelastic instabilities with a nonlinear absorber was also analyzed [10–12].

---

\*Corresponding author

Analytical models have also shown the sensitivity of a NES performance according to the values of its stiffness and damping parameters. However, it is very difficult to control and to identify the damping coefficient of a mechanical assembly during the design in order to have the full potential described by the analytical model. The consequences of an incorrect value of damping coefficient, which is not adjusted, is an important amplitude peak and even higher than that of the structure without absorber for frequencies lower than the natural frequency. This phenomenon called "detached resonance" is not due to a shift of a linear resonance, but to a branch of solutions due to nonlinear dynamics [13]. Therefore, it is important to identify and to adjust experimentally the right set of parameters.

The impact of an additional physics in the absorber has been studied recently with a research field on multiphysics absorbers which would involve passive electrical circuits to convert the mechanical energy from the vibrations into electrical energy. Nowadays, the studies on this type of absorbers are rather oriented toward energy harvesting [14–18]. In the present paper, an electrical circuit is used to create an equivalent mechanical damping, to overcome the unpredictability of the purely mechanical damping stemming from the assembly of the absorber.

This work illustrates the concept of a new type of nonlinear absorber with an electro-magnetomechanical coupling in order to demonstrate the possibility to adjust the equivalent damping of the absorber to improve its efficiency. In the first part, the prototype will be introduced. Then the analytical model of the system is presented to evaluate the performances of the potential of the electro-magnetomechanical coupling. The Complexification-Averaging (CX-A) technique and multi scale method [19] have been used to derive modulation equations, to compute the fixed point solutions and the slow invariant manifold. Finally, the analytical results and experimental tests with a vibration shaker will be presented and compared.

## 2. Electro-magnetomechanical coupling

### 2.1. Experimental setup

The design of the absorber consists of a mass-spring system nonlinearly coupled to the structure to be damped, represented as a linear oscillator (LO). The prototype in this study is presented in Figure 1. It consists of an LO composed of a mass of 64 kg connected to the ground by 4 springs. The LO is connected to an excitation shaker transmitting a dynamic excitation. The mechanical components of the absorber are a moving mass of 1.4 kg positioned on the LO, it is the absorber. It translates along two slides by means of linear bearings. The restoring force of the absorber is generated by the four springs which are mounted on pivots on the LO and the absorber, so they only undertake traction forces. The trajectory of the springs, shown in Figure 2, leads to a mostly nonlinear cubic stiffness, comprising a residual linear term due to a slight elongation during their installation. The nonlinear restoring force is given by the following equation.

$$f_{nl}(x) = k_{2l}x + k_{2c}x^3 \quad (1)$$

with

$$k_{2l} = \frac{2P}{l} + 2k \left( 1 - \frac{l}{l_0} \right), \quad k_{2c} = \frac{kl_0}{l^3} - \frac{P}{l^3} \quad (2)$$

$k$  being the stiffness of the spring,  $P$  the preload applied to the spring and  $l_0$  its initial length.

The electro-magnetomechanical coupling is achieved by a coil / magnet assembly. The 80 mm long coil is placed on the top of the absorber. Being integral to the absorber, it moves around its associated magnetic bar fixed to the LO (Figure 1). The magnetic bar, slightly longer than the coil with 90 mm, is made up of 18 superimposed cylindrical magnets giving a modular magnet system. The interaction between the field of the magnet and the coil, stemming from their relative displacement, creates an electrical current. The field created by the coil varies according to the resistance which is applied to its terminals. It can be configured in open circuit (infinite resistance) or in closed circuit (almost zero resistance).

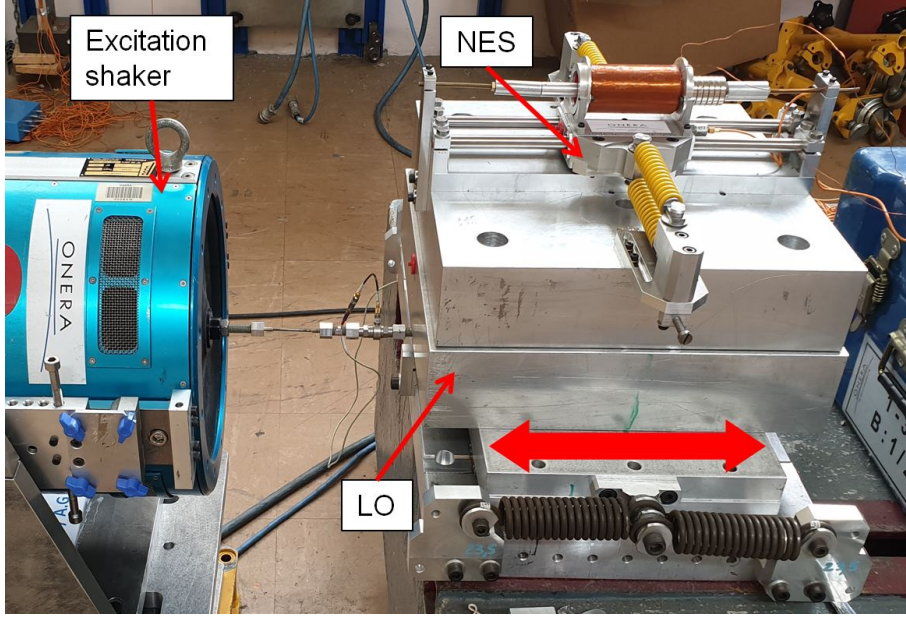


Figure 1: Prototype of the absorber with the magnet-coil system

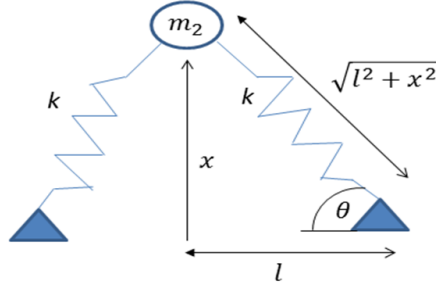


Figure 2: Springs configuration causing nonlinear stiffness

The complete system is a 2-DOF model made up of the LO, described by a mass  $m_1$ , a stiffness  $k_1$  and a damping coefficient  $c_1$ . The LO is coupled to the absorber, described by a mass  $m_2$ , a cubic stiffness  $k_{2c}$ , a linear stiffness  $k_{2l}$  and a damping coefficient  $c_2$ . The values of these different parameters of the system are presented in TABLE1. An excitation force  $F_e \sin(\bar{\Omega}t)$  is applied to the LO. A diagram of this system is presented in Figure 3. As a reminder, in the assembly, the magnet is fixed to the main structure, while the coil is fixed to the absorber (Figure 4). As a result the magnet displacement is  $x_m = x_1$ ,  $x_1$  being the displacement of the LO, and the coil displacement is  $x_c = x_2$ ,  $x_2$  being the displacement of the absorber. The equations of movement characterizing this assembly taking into account the electro-magnetomechanical coupling are

$$\left\{ \begin{array}{l} m_1 \frac{d^2 x_1}{dt^2} + c_1 \frac{dx_1}{dt} + k_1 x_1 + c_2 \left( \frac{dx_1}{dt} - \frac{dx_2}{dt} \right) + k_{2l} (x_1 - x_2) + k_{2c} (x_1 - x_2)^3 = F_e \sin(\bar{\Omega}t) \\ m_2 \frac{d^2 x_2}{dt^2} + c_2 \left( \frac{dx_2}{dt} - \frac{dx_1}{dt} \right) + k_{2l} (x_2 - x_1) + k_{2c} (x_1 - x_2)^3 - \theta(y) I = 0 \\ L_c \frac{dI}{dt} + (R_c + R_i) I + \theta(y) \dot{y} = 0 \end{array} \right. \quad (3)$$

Parameter	Value	Parameter	Value
$m_1$ [kg]	64	$m_2$ [kg]	1.4
$c_1$ [N/m.s <sup>-1</sup> ]	97	$c_2$ [N/m.s <sup>-1</sup> ]	1
$k_1$ [N.m <sup>-1</sup> ]	91324	$k_{2l}$ [N.m <sup>-1</sup> ]	500
-	-	$k_{2c}$ [N.m <sup>-3</sup> ]	8.44.10 <sup>6</sup>

Table 1: Parameters of the system

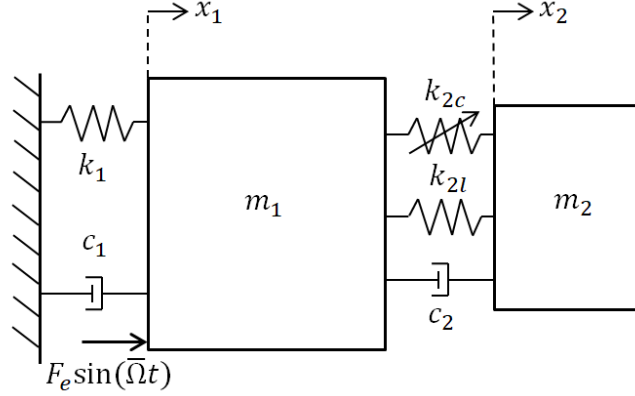


Figure 3: A linear principal oscillator coupled to an NES

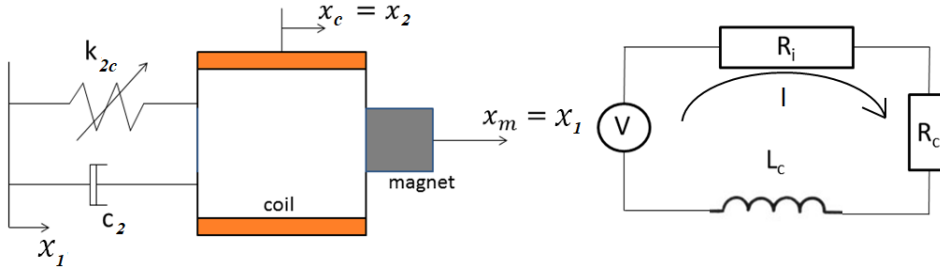


Figure 4: Coupled system: mechanical and electrical representations

$L_c$ ,  $R_c$ ,  $R_i$  and  $I$  are respectively the coil inductance, the coil resistance, the resistance applied to its terminals and the current. The term  $\theta(y)$  is called the electro-magnetomechanical coupling coefficient where  $y = x_m - x_c$  the displacement between the coil and the magnet.

## 2.2. Modelling of the electro-magnetomechanical coupling

In the literature, this electro-magnetomechanical coupling term is often considered constant for the coil-magnet interaction. However, Sneller A.J. and al. [20] showed that the coupling term between these components evolves nonlinearly with respect to their relative initial position. It is therefore important to take this variation into account. In this part, their model is used to find the configuration where the coupling

is the more important for low displacements. According to Faraday's law, a voltage  $V$  is created across a coil, proportional to the magnetic flux variation  $\Phi$  which crosses it.

$$V = -\frac{d\Phi}{dt} = -\frac{d\Phi}{dx} \frac{dx}{dt} \quad (4)$$

The model allows to calculate the voltage and nonlinear electromagnetic coupling between a coil and an oscillating magnet inside. The expression for the voltage function of the displacement between the coil and the magnet  $y = x_m - x_c$  is

$$V = \theta(y)\dot{y} \quad (5)$$

$$\theta(y) = -\frac{N_c B_r \nu_s \xi}{2A_c} \sum_{i,j=1}^2 (-1)^{i+j} \left[ \ln(r_i + z_{ij}) - \frac{r_i}{z_{ij}} \right] \quad (6)$$

with  $z_{ij}^2 = r_i^2 + (x'_{cj} + y)^2$ ,  $x'_{c1} = -L/2$  and  $x'_{c2} = L/2$ . The following example will show that the electromagnetomechanical coupling strongly depends on the distance between the coil and the magnet.

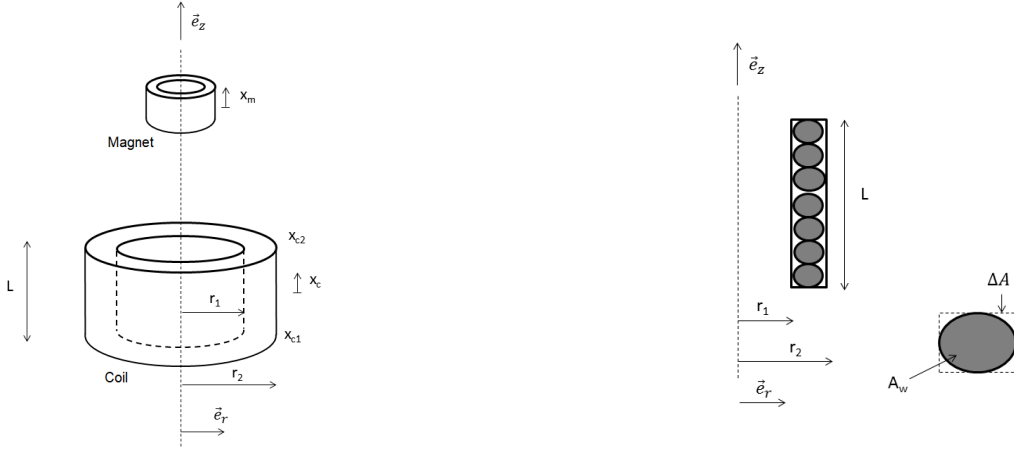


Figure 5: Magnet-coil interaction and polar cross section of a coil

Parameter	Value	Unit
Internal coil diameter ( $2r_1$ )	33	mm
External coil diameter ( $2r_2$ )	41.2	mm
Coil length ( $L$ )	80.4	mm
Coil resistance ( $R_c$ )	11.6	$\Omega$
Coil inductance ( $L_c$ )	14.25	mH
Number of turns ( $N_c$ )	1088	
Wire diameter	0.5	mm
Coil filling $\xi_c$	65	%
Magnet remanence ( $B_r$ )	1.32	T
Magnet volume ( $\nu_s$ )	$4, 3.10^{-5}$	$\text{m}^3$

Table 2: Parameters of the coil-magnet system

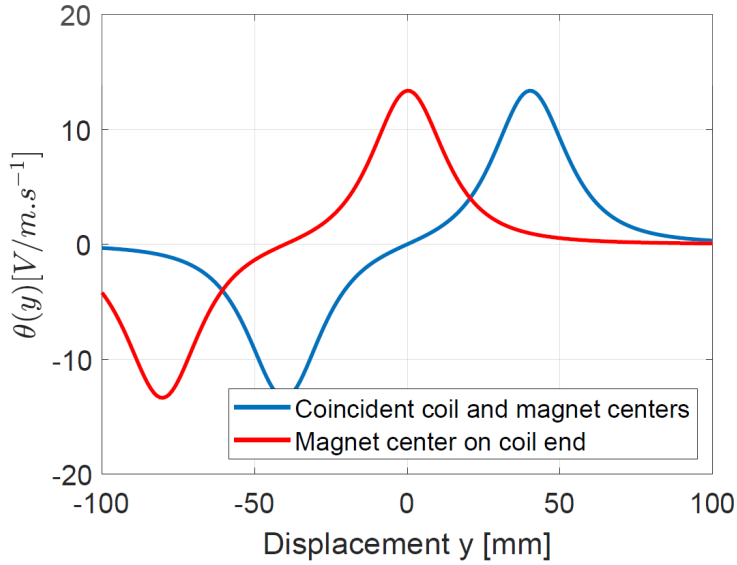


Figure 6: Magneto-mechanical coupling term  $\theta(y)$

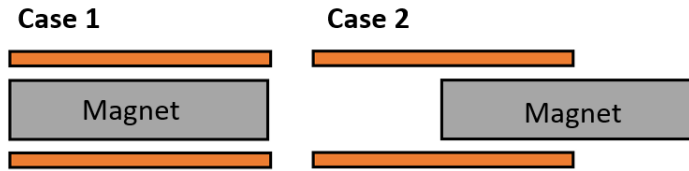


Figure 7: Different configurations of the magnet into the coil

Figure 6 depicts the evolution of the coupling term  $\theta(y)$  simulated for different configurations. The first configuration (blue curve) represents the case where the centroids of the magnet and coil coincide (Figure 7 case 1). The coupling is very weak for the small displacements. However, it is desirable that this coupling is maximised from the very onset of movement to dissipate the vibrational energy even for small amplitude displacements. The distance between one of the extrema of the blue curve and the ordinate axis corresponds to the distance between the centroid of the magnet and one end of the coil. To achieve an optimal efficiency even for low displacements, the second configuration (red curve Figure 6 and case 2 Figure 7) where the magnet moves at the end of the coil seems the most efficient one and is chosen for the study.

### 3. Modeling of the complete system

#### 3.1. Analytical solution of the equations of movement

As a reminder, the equations of movement characterizing the complete assembly taking into account the electro-magnetomechanical coupling are

$$\left\{ \begin{array}{l} m_1 \frac{d^2 x_1}{dt^2} + c_1 \frac{dx_1}{dt} + k_1 x_1 + c_2 \left( \frac{dx_1}{dt} - \frac{dx_2}{dt} \right) + k_{2l}(x_1 - x_2) + k_{2c}(x_1 - x_2)^3 = F_e \sin(\bar{\Omega}t) \\ m_2 \frac{d^2 x_2}{dt^2} + c_2 \left( \frac{dx_2}{dt} - \frac{dx_1}{dt} \right) + k_{2l}(x_2 - x_1) + k_{2c}(x_1 - x_2)^3 - \theta(y) I = 0 \\ L_c \frac{dI}{dt} + (R_c + R_i) I + \theta(y) \dot{y} = 0 \end{array} \right. \quad (7)$$

An approximation is calculated analytically by assuming the term  $L_c \frac{dI}{dt}$  is negligible for low frequencies and low amplitudes. Unfortunately, this point has not been verified by experimental measurements of the intensity because of the insufficient sensitivity of our devices. However, a temporal solution of the system with or without this term on Matlab confirmed this approximation. So, it is possible to write

$$L_c \frac{dI}{dt} = 0 \longrightarrow (R_c + R_i) I + \theta(y) \dot{y} = 0 \quad (8)$$

It is then possible to write the second equation of (7) in the form

$$m_2 \frac{d^2 x_2}{dt^2} + \left( c_2 + \frac{\theta^2(y)}{R_c + R_i} \right) \left( \frac{dx_2}{dt} - \frac{dx_1}{dt} \right) + k_{2l}(x_2 - x_1) + k_{2c}(x_2 - x_1)^3 = 0 \quad (9)$$

This equation shows the existence of an equivalent damping coefficient, of two natures : mechanical and electromagnetic. The damping is controlled with the applied resistance, the higher the applied resistance  $R_i$  the more the damping term  $\frac{\theta^2(y)}{R_c + R_i}$  created by the coil/magnet assembly decreases, until it tends towards a purely mechanical damping and it becomes maximum for  $R_i$  zero.

The analytical study of the dynamics of the multi-physics absorber coupled to a linear oscillator is presented by the complexification and multi-scale methods. The equations of motion describing the model are

$$\left\{ \begin{array}{l} m_1 \frac{d^2 x_1}{dt^2} + c_1 \frac{dx_1}{dt} + k_1 x_1 + c_2 \left( \frac{dx_1}{dt} - \frac{dx_2}{dt} \right) + k_{2l}(x_1 - x_2) + k_{2c}(x_1 - x_2)^3 = F_e \sin(\bar{\Omega}t) \\ m_2 \frac{d^2 x_2}{dt^2} + \left( c_2 + \frac{\theta^2(y)}{R_c + R_i} \right) \left( \frac{dx_2}{dt} - \frac{dx_1}{dt} \right) + k_{2l}(x_2 - x_1) + k_{2c}(x_2 - x_1)^3 = 0 \end{array} \right. \quad (10)$$

With  $\bar{\Omega}$  the applied frequency. In the previous part, the model describing the multi-physics coupling was introduced. Due to its complex expression and the difficulty to introduce it into the analytical solution, a simplification of this law is made using the following expression

$$\theta(y) = a_1 y^8 + a_2 y^6 + a_3 y^4 + a_4 y^2 + a_5 \quad (11)$$

The graphical representation of this approximation is shown in figure 8. Then, the following change of variables is introduced

$$\begin{aligned} \varepsilon &= \frac{m_2}{m_1}, \quad \omega_0^2 = \frac{k_1}{m_1}, \quad K_1 = \frac{k_{2l}}{m_2 \omega_0^2}, \quad K_3 = \frac{k_{2c}}{m_2 \omega_0^2}, \quad \lambda_1 = \frac{c_1}{m_2 \omega_0}, \\ \lambda_2 &= \frac{c_2}{m_2 \omega_0}, \quad \Omega = \frac{\bar{\Omega}}{\omega_0}, \quad \tau = \omega_0 t, \quad \frac{\theta^2(y)}{m_2 \omega_0 (R_c + R_i)} = \sum_{i=1}^9 \gamma_i y^{18-2i} \end{aligned} \quad (12)$$

By substituting (12) in the equations (10), the equilibrium reads

$$\left\{ \begin{array}{l} \ddot{x}_1 + \varepsilon \lambda_1 \dot{x}_1 + \varepsilon \lambda_2 (\dot{x}_1 - \dot{x}_2) + x_1 + \varepsilon K_1 (x_1 - x_2) + \varepsilon K_3 (x_1 - x_2)^3 = \varepsilon F \sin(\Omega \tau) \\ \ddot{x}_2 + \left( \lambda_2 + \sum_{i=1}^9 \gamma_i y^{18-2i} \right) (\dot{x}_2 - \dot{x}_1) + K_1 (x_2 - x_1) + K_3 (x_2 - x_1)^3 = 0 \end{array} \right. \quad (13)$$



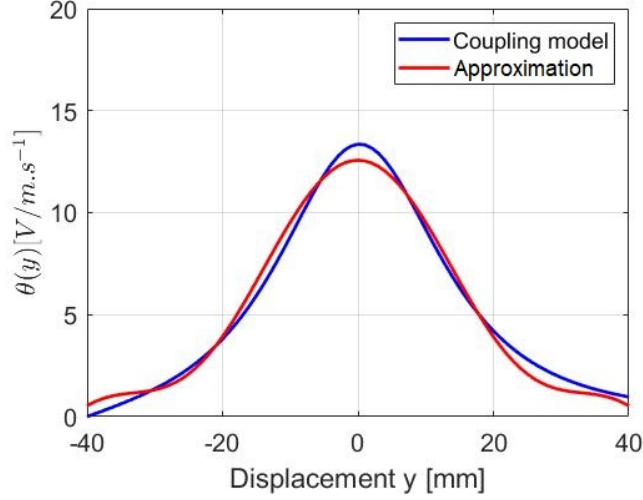


Figure 8: Simplification of the electro-magnetomechanical coupling model

The dots (  $\dot{\phantom{x}}$  ) represent the derivatives with respect to the dimensionless time  $\tau$ . Now, the barycentric coordinates is introduced

$$v = x_1 + \varepsilon x_2, \quad w = x_1 - x_2 \quad (14)$$

Then, (14) is introduced into (13), giving the following system

$$\begin{cases} \ddot{v} + \varepsilon \lambda_1 \frac{\dot{v} + \varepsilon \dot{w}}{1 + \varepsilon} + \frac{v + \varepsilon w}{1 + \varepsilon} - \varepsilon \left( \sum_{i=1}^9 \gamma_i w^{18-2i} \right) \dot{w} = \varepsilon F \sin(\Omega \tau) \\ \ddot{w} + \varepsilon \lambda_1 \frac{\dot{v} + \varepsilon \dot{w}}{1 + \varepsilon} + \frac{v + \varepsilon w}{1 + \varepsilon} + \lambda_2 (1 + \varepsilon) \dot{w} + \left( \sum_{i=1}^9 \gamma_i w^{18-2i} \right) \dot{w} \\ \quad + K_1 (1 + \varepsilon) w + K_3 (1 + \varepsilon) w^3 = \varepsilon F \sin(\Omega \tau) \end{cases} \quad (15)$$

The cubic nonlinearity of the stiffness and the multiphysics coupling in the second equation of the system does not allow an exact analytical solution. An approximation of periodic solutions is calculated by a combination of complexification methods and multiple scales. The system is supposed to follow a 1:1 resonance, meaning that the main oscillator and the NES oscillate at the same excitation frequency  $\Omega$ . It is shown that this energy transfer is defined as a 1:1 resonance capture (LO and NES oscillate at the same frequency) between the primary system and the NES[21, 21, 22]. First, the following complex variables is introduced

$$\begin{aligned} \Psi_1 &= \dot{v} + i\Omega v, \quad \Psi_2 = \dot{w} + i\Omega w \\ \Psi_1 &= \phi_1 \exp(i\Omega \tau), \quad \Psi_2 = \phi_2 \exp(i\Omega \tau) \end{aligned} \quad (16)$$

The following equivalences are valid

$$\begin{cases} v = \frac{1}{2i\Omega} (\Psi_1 - \Psi_1^*), \quad w = \frac{1}{2i\Omega} (\Psi_2 - \Psi_2^*) \\ \dot{v} = \frac{1}{2} (\Psi_1 + \Psi_1^*), \quad \dot{w} = \frac{1}{2} (\Psi_2 + \Psi_2^*) \\ \ddot{v} = \dot{\Psi}_1 - \frac{i\Omega}{2} (\Psi_1 + \Psi_1^*), \quad \ddot{w} = \dot{\Psi}_2 - \frac{i\Omega}{2} (\Psi_2 + \Psi_2^*) \end{cases} \quad (17)$$

The addition of the complex variables leads to partitioning the fast oscillations of the system at the excitation frequency  $\Omega$  and the slow modulation of the complex amplitudes  $\{\phi_1, \phi_2\}$ . By injecting (17) into (15), the following system is obtained

$$\left\{ \begin{array}{l} \dot{\Psi}_1 - \frac{i\Omega}{2}(\Psi_1 + \Psi_1^*) + \frac{\varepsilon}{1+\varepsilon}\lambda_1 \left( \frac{1}{2}(\Psi_1 + \Psi_1^*) + \frac{\varepsilon}{2}(\Psi_2 + \Psi_2^*) \right) + \frac{1}{2i\Omega(1+\varepsilon)} \left( \Psi_1 + \Psi_1^* + \frac{\varepsilon}{2}(\Psi_2 + \Psi_2^*) \right) \\ - \left( \frac{\gamma_1}{65536\Omega^{16}}(\Psi_2 - \Psi_2^*)^{16} - \frac{\gamma_2}{16384\Omega^{14}}(\Psi_2 - \Psi_2^*)^{14} + \frac{\gamma_3}{4096\Omega^{14}}(\Psi_2 - \Psi_2^*)^{12} - \frac{\gamma_4}{1024\Omega^{10}}(\Psi_2 - \Psi_2^*)^{10} \right. \\ \left. + \frac{\gamma_5}{256\Omega^8}(\Psi_2 - \Psi_2^*)^8 - \frac{\gamma_6}{64\Omega^6}(\Psi_2 - \Psi_2^*)^6 + \frac{\gamma_7}{16\Omega^4}(\Psi_2 - \Psi_2^*)^4 - \frac{\gamma_8}{4\Omega^2}(\Psi_2 - \Psi_2^*)^2 + \gamma_9 \right) \frac{\varepsilon}{2}(\Psi_2 + \Psi_2^*) \\ = \varepsilon F \sin(\Omega\tau) \\ \\ \dot{\Psi}_2 - \frac{i\Omega}{2}(\Psi_2 + \Psi_2^*) + \frac{\varepsilon}{1+\varepsilon}\lambda_1 \left( \frac{1}{2}(\Psi_1 + \Psi_1^*) + \frac{\varepsilon}{2}(\Psi_2 + \Psi_2^*) \right) + \frac{1}{2i\Omega(1+\varepsilon)} \left( \Psi_1 + \Psi_1^* + \frac{\varepsilon}{2}(\Psi_2 + \Psi_2^*) \right) \\ + \left( \frac{\gamma_1}{65536\Omega^{16}}(\Psi_2 - \Psi_2^*)^{16} - \frac{\gamma_2}{16384\Omega^{14}}(\Psi_2 - \Psi_2^*)^{14} + \frac{\gamma_3}{4096\Omega^{14}}(\Psi_2 - \Psi_2^*)^{12} - \frac{\gamma_4}{1024\Omega^{10}}(\Psi_2 - \Psi_2^*)^{10} \right. \\ \left. + \frac{\gamma_5}{256\Omega^8}(\Psi_2 - \Psi_2^*)^8 - \frac{\gamma_6}{64\Omega^6}(\Psi_2 - \Psi_2^*)^6 + \frac{\gamma_7}{16\Omega^4}(\Psi_2 - \Psi_2^*)^4 - \frac{\gamma_8}{4\Omega^2}(\Psi_2 - \Psi_2^*)^2 + \gamma_9 \right) \frac{1}{2}(\Psi_2 + \Psi_2^*) \\ + \frac{\lambda_2}{2}(1+\varepsilon)(\Psi_2 + \Psi_2^*) + \frac{K_1}{2i\Omega}(\Psi_2 - \Psi_2^*) + \frac{iK_3}{8\Omega^3}(\Psi_2 - \Psi_2^*)^3 = \varepsilon F \sin(\Omega\tau) \end{array} \right. \quad (18)$$

Then, the equations are averaged over the fast time scale. Therefore, only terms proportional to  $\exp(i\Omega\tau)$  are kept. The  $\Psi_i$  terms are replaced with  $\phi_i \exp(i\Omega\tau)$ . A system proportional to  $\phi_1$  and  $\phi_2$  is established

$$\left\{ \begin{array}{l} \dot{\phi}_1 - \frac{i\Omega}{2}\phi_1 + \frac{\varepsilon\lambda_1}{2(1+\varepsilon)}(\phi_1 + \varepsilon\phi_2) - \frac{i}{2\Omega(1+\varepsilon)}(\phi_1 + \varepsilon\phi_2) - \frac{715\varepsilon\gamma_1}{65536\Omega^{16}}|\phi_2|^{16}\phi_2 - \frac{429\varepsilon\gamma_2}{32768\Omega^{14}}|\phi_2|^{14}\phi_2 \\ - \frac{33\varepsilon\gamma_3}{2048\Omega^{12}}|\phi_2|^{12}\phi_2 - \frac{21\varepsilon\gamma_4}{1024\Omega^{10}}|\phi_2|^{10}\phi_2 - \frac{7\varepsilon\gamma_5}{256\Omega^8}|\phi_2|^8\phi_2 - \frac{5\varepsilon\gamma_6}{128\Omega^6}|\phi_2|^6\phi_2 - \frac{\varepsilon\gamma_7}{16\Omega^4}|\phi_2|^4\phi_2 \\ - \frac{\varepsilon\gamma_8}{8\Omega^2}|\phi_2|^2\phi_2 - \frac{\varepsilon\gamma_9}{2}\phi_2 + \frac{i\varepsilon F}{2} = 0 \\ \\ \dot{\phi}_2 - \frac{i\Omega}{2}\phi_2 + \frac{\varepsilon\lambda_1}{2(1+\varepsilon)}(\phi_1 + \varepsilon\phi_2) - \frac{i}{2\Omega(1+\varepsilon)}(\phi_1 + \varepsilon\phi_2) + \frac{\lambda_2}{2}(1+\varepsilon)\phi_2 - (1+\varepsilon)\frac{iK_1}{2\Omega}\phi_2 \\ - (1+\varepsilon)\frac{i3K}{8\Omega^3}|\phi_2|^2\phi_2 + \frac{715\gamma_1}{65536\Omega^{16}}|\phi_2|^{16}\phi_2 + \frac{429\gamma_2}{32768\Omega^{14}}|\phi_2|^{14}\phi_2 + \frac{33\gamma_3}{2048\Omega^{12}}|\phi_2|^{12}\phi_2 + \frac{21\gamma_4}{1024\Omega^{10}}|\phi_2|^{10}\phi_2 \\ + \frac{7\gamma_5}{256\Omega^8}|\phi_2|^8\phi_2 + \frac{5\gamma_6}{128\Omega^6}|\phi_2|^6\phi_2 + \frac{\gamma_7}{16\Omega^4}|\phi_2|^4\phi_2 + \frac{\gamma_8}{8\Omega^2}|\phi_2|^2\phi_2 + \frac{\gamma_9}{2}\phi_2 + \frac{i\varepsilon F}{2} = 0 \end{array} \right. \quad (19)$$

Since  $\phi_1$  and  $\phi_2$  are the slow evolutions of the amplitudes for a 1:1 type resonance, the temporal evolution of the LO-NES system is governed by the system of equations (19) considering a periodic oscillation of the two oscillators at the same frequency  $\Omega$ .

### 3.2. Fixed point solutions

From (19), it is possible to determine the fixed point solutions. The latter corresponds to the periodic solutions of system (15) under the assumption of a 1:1 resonance. They are calculated by finding the zeros of (19)

$$\dot{\phi}_1 = \dot{\phi}_2 = 0 \longrightarrow \phi_1(\tau) = \phi_{10}, \quad \phi_2(\tau) = \phi_{20} \quad (20)$$

By introducing (20) into (19), the expression of  $\phi_{10}$  is calculated as a function of  $\phi_{20}$  and system parameters.

$$\begin{aligned} \phi_{10} = & \beta_1|\phi_{20}|^{16}\phi_{20} + \beta_2|\phi_{20}|^{14}\phi_{20} + \beta_3|\phi_{20}|^{12}\phi_{20} + \beta_4|\phi_{20}|^{10}\phi_{20} + \beta_5|\phi_{20}|^8\phi_{20} \\ & + \beta_6|\phi_{20}|^6\phi_{20} + \beta_7|\phi_{20}|^4\phi_{20} + \beta_8|\phi_{20}|^2\phi_{20} + \beta_9 + \phi_{20} + \beta_{10} \end{aligned} \quad (21)$$

By injecting (21) into the second equation of (19), it is possible to obtain the following expression

$$\begin{aligned} & A|\phi_{20}|^{16}\phi_{20} + B|\phi_{20}|^{14}\phi_{20} + C|\phi_{20}|^{12}\phi_{20} + D|\phi_{20}|^{10}\phi_{20} + E|\phi_{20}|^8\phi_{20} \\ & + F|\phi_{20}|^6\phi_{20} + G|\phi_{20}|^4\phi_{20} + H|\phi_{20}|^2\phi_{20} + I\phi_{20} + J = 0 \end{aligned} \quad (22)$$

Where  $A$ ,  $B$  and  $C$  are coefficients which depend on the parameters of the system. By setting  $\phi_{20} = |\phi_{20}| \exp(i\theta)$  and some mathematical manipulations, a polynomial of order 17 is expressed

$$\sum_{i=0}^{17} \alpha_i Z_{20}^i = 0, \quad Z_{20} = |\phi_{20}|^2 \quad (23)$$

With  $\alpha_i$  real coefficients depending on the parameters of the system. The analytical solution of this polynomial allows to calculate the modulus  $|\phi_{20}|$ , then  $\phi_{20}$  and  $\phi_{10}$  by going up in (22) and (20).

It is possible to plot an equivalent of the FRF (Frequency Response Function) by plotting the evolution of the amplitude of the stationary responses (fixed points) as a function of the frequency. It will be used in the next part to analyse the dynamic behavior of the system. The stability of fixed points is studied by adding small disturbances around them

$$\phi_1(\tau) = \phi_{10} + \rho_1(\tau), \quad \phi_2(\tau) = \phi_{20} + \rho_2(\tau) \quad (24)$$

Then, (24) is introduced in (19) and only the terms proportional to  $\phi_i$  are kept. It results after some mathematical arrangements, to the following relation

$$\begin{bmatrix} \dot{\rho}_1 \\ \dot{\rho}_2 \\ \dot{\rho}_1^* \\ \dot{\rho}_2^* \end{bmatrix} \begin{bmatrix} M_{11} & \varepsilon M_{21} & 0 & 0 \\ M_{21} & M_{22} & 0 & M_{24} \\ 0 & 0 & M_{11}^* & \varepsilon M_{21}^* \\ 0 & M_{24}^* & M_{21}^* & M_{22}^* \end{bmatrix} = \begin{bmatrix} \rho_1 \\ \rho_2 \\ \rho_1^* \\ \rho_2^* \end{bmatrix} + C \quad (25)$$

The stability of the fixed points is determined by the computation of the eigenvalues of the matrix (25). If the eigenvalues are negative reals, then the fixed point is stable. If a real eigenvalue crosses the complex half-plane, the fixed point is then a saddle-node. Finally, if a pair of conjugate complex eigenvalues leaves from the left of the complex half-plane, it leads to a Hopf bifurcation.

### 3.3. Asymptotic study

In order to study the energy transfer, an asymptotic analysis by the method of multiple scales is carried out because the mass ratio  $\varepsilon$  with a NES, is very low,  $\varepsilon \ll 1$  [8]. First of all, the time  $\tau$  is decomposed into several sub-scales of time, increasingly smaller. The derivation is a sequence of partial derivatives :

$$\frac{\partial}{\partial \tau} = \frac{\partial}{\partial \tau_0} + \varepsilon \frac{\partial}{\partial \tau_1} + \varepsilon^2 \frac{\partial}{\partial \tau_2} + \dots, \quad \tau_k = \varepsilon^k \tau, \quad k = 0, 1, 2, \dots \quad (26)$$

The solutions is also expressed as a polynomial of  $\varepsilon$  :

$$\begin{cases} \phi_1(\tau_0, \tau_1, \dots) = \phi_{10} + \varepsilon \phi_{11} + 0(\varepsilon), & \frac{\partial \phi_1}{\partial \tau} = \frac{\partial \phi_{10}}{\partial \tau_0} + \varepsilon \left( \frac{\partial \phi_{11}}{\partial \tau_0} + \frac{\partial \phi_{10}}{\partial \tau_1} \right) + 0(\varepsilon) \\ \phi_2(\tau_0, \tau_1, \dots) = \phi_{20} + \varepsilon \phi_{21} + 0(\varepsilon), & \frac{\partial \phi_2}{\partial \tau} = \frac{\partial \phi_{20}}{\partial \tau_0} + \varepsilon \left( \frac{\partial \phi_{21}}{\partial \tau_0} + \frac{\partial \phi_{20}}{\partial \tau_1} \right) + 0(\varepsilon) \end{cases} \quad (27)$$

The equations (26) and (27) are introduced in (19). Terms proportional to  $\varepsilon^0$  are gathered.

$$\varepsilon^0 : \begin{cases} \frac{\partial \phi_{10}}{\partial \tau_0} = 0 \\ \frac{\partial \phi_{20}}{\partial \tau_0} + \frac{\lambda_2}{2} \phi_{20} + \frac{i}{2} (\phi_{20} - \phi_{10}) - \frac{iK_1}{2} \phi_{20} - \frac{3}{8} iK_3 |\phi_{20}|^2 \phi_{20} + \frac{715\gamma_1}{65536\Omega^{16}} |\phi_{20}|^{16} \phi_{20} \\ + \frac{429\gamma_2}{32768\Omega^{14}} |\phi_{20}|^{14} \phi_{20} + \frac{33\gamma_3}{2048\Omega^{12}} |\phi_{20}|^{12} \phi_{20} + \frac{21\gamma_4}{1024\Omega^{10}} |\phi_{20}|^{10} \phi_{20} + \frac{7\gamma_5}{256\Omega^8} |\phi_{20}|^8 \phi_{20} \\ + \frac{3\gamma_6}{128\Omega^6} |\phi_{20}|^6 \phi_{20} + \frac{7\gamma_7}{16\Omega^4} |\phi_{20}|^4 \phi_{20} + \frac{7\gamma_8}{8\Omega^2} |\phi_{20}|^2 \phi_{20} + \frac{79}{2} \phi_{20} = 0 \end{cases} \quad (28)$$

It is important to note that at the first time scale  $\tau_0$ , the amplitude modulations are independent of the excitation force. Indeed, this force only appears at the slower time scale  $\tau_1 = \varepsilon^1 \tau$ . The equations at the scale  $\varepsilon^0$  are rewritten in the polar form :

$$\phi_{10} = N_{10} \exp(i\theta_{10}), \quad \phi_{20} = N_{20} \exp(i\theta_{20}) \quad (29)$$

The following system of equations is then obtained :

$$\begin{cases} \frac{\partial N_{10}}{\partial \tau} = 0 \\ \frac{\partial N_{20}}{\partial \tau} = -\frac{\lambda_2}{2} N_{20} + \frac{N_{10}}{2} \sin(\theta_0) - \frac{715\gamma_1}{65536} N_{20}^{17} - \frac{429\gamma_2}{32768} N_{20}^{15} - \frac{33\gamma_3}{2048} N_{20}^{13} - \frac{21\gamma_4}{1024} N_{20}^{11} - \frac{7\gamma_5}{256} N_{20}^9 \\ - \frac{5\gamma_6}{128} N_{20}^7 - \frac{7\gamma_7}{16} N_{20}^5 - \frac{7\gamma_8}{8} N_{20}^3 - \frac{7\gamma_9}{2} N_{20} \\ \frac{\partial \theta_0}{\partial \tau} = \frac{N_{10}}{2N_{20}} \cos(\theta_0) - \frac{1}{2} + \frac{K_1}{2} + \frac{3}{8} K_3 N_{20}^2 \end{cases} \quad (30)$$

With  $\theta_0 = \theta_{20} - \theta_{10}$ . The equilibrium equations are given by :

$$\begin{cases} \sin(\theta_0) = \frac{1}{N_{10}} (\lambda_2 N_{20} + \frac{715\gamma_1}{32768} N_{20}^{17} + \frac{429\gamma_2}{16384} N_{20}^{15} + \frac{33\gamma_3}{1024} N_{20}^{13} + \frac{21\gamma_4}{512} N_{20}^{11} + \frac{7\gamma_5}{128} N_{20}^9 \\ + \frac{5\gamma_6}{64} N_{20}^7 + \frac{7\gamma_7}{8} N_{20}^5 + \frac{7\gamma_8}{4} N_{20}^3 + \gamma_9 N_{20}) \\ \cos(\theta_0) = \frac{N_{20}}{N_{10}} (1 - K_1 - \frac{3}{4} K_3 N_{20}^2) \end{cases} \quad (31)$$

By squaring the equations and then adding them, the fixed points of the system satisfy the equation :

$$\begin{aligned} N_{10}^2 = N_{20}^2 \left( 1 - K_1 - \frac{3}{4} K_3 N_{20}^2 \right) + (\lambda_2 N_{20} + \frac{715\gamma_1}{32768} N_{20}^{17} + \frac{429\gamma_2}{16384} N_{20}^{15} + \frac{33\gamma_3}{1024} N_{20}^{13} \\ + \frac{21\gamma_4}{512} N_{20}^{11} + \frac{7\gamma_5}{128} N_{20}^9 + \frac{5\gamma_6}{64} N_{20}^7 + \frac{7\gamma_7}{8} N_{20}^5 + \frac{7\gamma_8}{4} N_{20}^3 + \gamma_9 N_{20}) \end{aligned} \quad (32)$$

With  $Z = N_{20}^2$ . This equation defines the Slow Invariant Manifold (SIM) of the system, it allows the relation between the parameters of the system which characterizes the dynamics of this one including its amplitude. For a fixed value of  $N_{10}$ , the polynomial of degree 3 is solved analytically. For each value of  $N_{10}$ , one to three positive solutions for  $N_{20}$  are found. To determine the stability of the solutions of the invariant variety, it is necessary to study the eigenvalues of the corresponding stability matrix. Figure 9 presents an example of the SIM for the case of a NES with the electro-magnetomechanical coupling when the resistance is minimal  $R_{min}$ .

Each possible solution is represented by a circle. The curve suggests three distinct zones. First at low amplitude, where the displacement of the LO is between 0 and 3.2 mm, only one stable solution (blue circles) exists for the periodic amplitude of the NES and the LO, there is a resonance 1:1, otherwise known as Constant Response Amplitude (CAR). The NES has almost the same amplitude as the LO, the slope is approximately 1. In this zone, the NES is inactive because it follows only the movement of the LO.

Between 3.2 and 3.7 mm LO displacement amplitude, starting from a first bifurcation point  $B_1$ , there are 3 branches of solutions: 2 stable separated by an unstable one. These solutions are differentiated by the amplitude of the NES: the low amplitudes and the highest amplitudes for the stable solutions and the intermediate amplitudes for the unstable. This typical configuration of nonlinear dynamics is at the origin of a movement generating relaxation cycles. For an amplitude value of LO, the system is first attracted to the lower amplitude solution of the NES, but a quick jump to the higher amplitude branch occurs. On this last branch, the NES dissipates much more energy through the damping coefficient  $c_2$  for a similar amplitude of the LO. However, with this energy dissipation, the whole system loses energy and falls back on the low amplitude solution. Having returned to this branch, the system recovers vibratory energy again and its amplitude begins to increase again until the jump on the high-amplitude branch forming a cycle which repeats. This particular behavior is achieved by the presence of unstable solutions (red circles), surrounded by the two branches of stable solutions. This phenomenon called SMR (Strongly Modulated Response), is observed numerically and experimentally.

Finally, beyond 3.7 mm LO displacement, a second bifurcation point  $B_2$  is reached. As for the first zone, only one stable solution for the LO / NES pair is possible, but this time, the amplitude of the NES is much

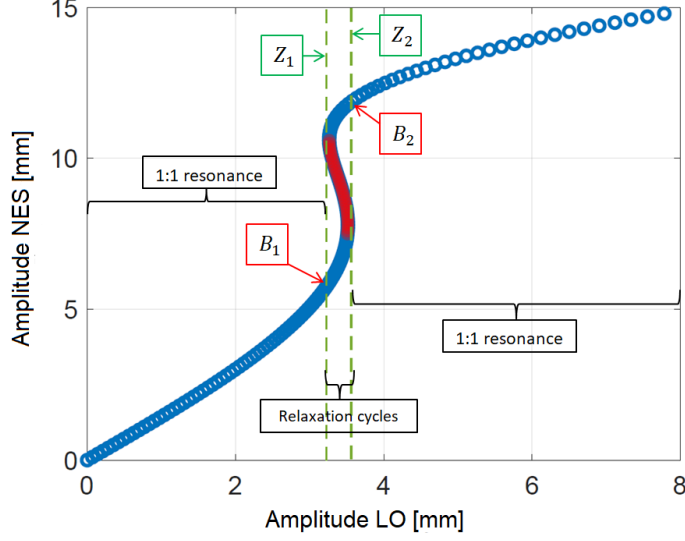


Figure 9: Slow Invariant Manifold (SIM) (blue circles: stable solutions, red circles: unstable solutions)

greater compared to LO. However, unlike the zone of relaxation cycles, the dynamics of the system is again a 1:1 CAR resonance and the slope is again around 1 heading towards a horizontal asymptote.

It is possible to identify the relaxation zone  $Z_1$  and  $Z_2$  analytically. These bounds are obtained by solving the invariant manifold equation to zero. Two remarks is made on these bounds. First, they both depend on the coefficient of the cubic stiffness coefficient  $K_3$  and the damping of the NES  $\lambda_2$ . It is necessary for  $Z_1$  that  $\lambda_2 < \sqrt{3}$  so that relaxation cycles can occur. Second, the activation threshold of the NES depends on the inverse of  $K_3$ . Therefore, a low threshold is obtained for high values of  $K_3$ . At first glance, it is possible to say the activation of the NES would be around the level of  $Z_2$  (if the NES has not undergone a disturbance, allowing it to jump to the higher branch). Because the amplitude jump takes place when the NES reaches the level of energy required. This point is verified using the calculation of fixed points.

#### 4. Study of the dynamical behavior of the multiphysics NES

##### 4.1. Analytical study

Now that the analytical model is set up, the NES with the addition of the electro-magneto-mechanical coupling will be studied using the fixed point solutions and the SIM. To begin with, the SIM of the NES in  $R_{inf}$  (infinite resistance - open electrical circuit) position and  $R_{min}$  (minimum resistance - closed circuit, only the internal resistance of the coil is considered) are plotted in Figure 10 in order to observe the variation in the dynamics of our system caused by the multi-physics coupling. As a reminder, the coupling increases the equivalent damping coefficient of the absorber. Two changes are noticeable when adding the coupling (NES +  $R_{min}$ ). First, a decrease in the three solutions area is caused. Then, an advance of this zone towards greater displacements of the LO, generating a greater activation threshold of the NES, going from 2.8 mm without coupling ( $R_{inf}$ ) to 3.7 mm. Moreover, in this figure, the SIM of the system with a damping coefficient  $c_2 = 12 \text{ N/m.s}^{-1}$  is drawn instead of that measured  $1 \text{ N/m.s}^{-1}$ . It is remarkable that the coupling makes it possible to obtain a SIM very similar of a system with a purely mechanical NES with a damping  $c_2 = 12 \text{ N/m.s}^{-1}$ .

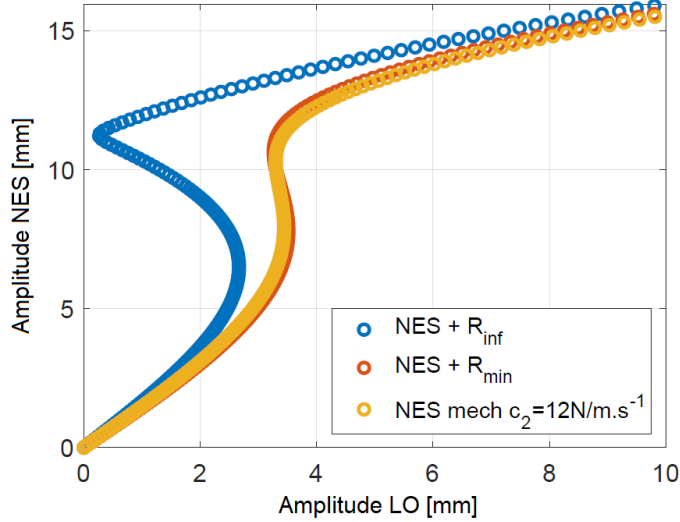


Figure 10: Slow Invariant Manifold of different NES configurations

First of all, the classic mechanical NES, without the addition of multiphysics coupling, is studied using fixed point solutions in order to understand the different behaviors of the NES according to the level of excitation and to observe the importance of the damping coefficient. First, the results for a solicitation  $F_e = 5N$  are presented in Figure 11. The figure introduces the analytical evolution of the LO when the NES is locked in gray and when the NES is released in blue. In both cases, a linear dynamic response is obtained with a similar amplitude of about 1.6 mm. The NES is then inactive. This result is explained by the previous SIM where it is shown that the activation threshold of the absorber without multi-physics coupling (equivalent to the infinite resistance case ( $R_{inf}$ )) is about 2.8 mm. At 1.6 mm, the NES is on the low amplitude solutions branch if it has not been disturbed to make it jump to the high amplitude branch. In addition, on the low amplitude branch, the slope is slightly greater than 1, explaining a slight dissipation of energy by the absorber. If the dynamic excitation continues to increase, passing to  $F_e = 10$  N, the following frequency evolution is given in Figure 12.

This time, the LO with the NES shows a behavior typical of systems fitted with nonlinear vibration absorbers. First, the appearance of areas with multiple solutions of amplitudes for the same frequency, either unstable (+) or stable (o). The system will converge towards a stable solution if it is possible. A unique branch of unstable solutions appears around the resonance involving a transfer of energy between the structure and the absorber where the cycles of relaxations occur. The activation threshold identified by the SIM, 2.8 mm, is shown in Figure 12. It is possible to see for frequencies above resonance that the amplitude level respects this threshold from which the unstable branch of single solutions appears. This results in a beginning of attenuation of the vibration level when the NES is released.

However, another phenomenon is observed in Figure 12. An area, for frequencies lower than the natural frequency present several solutions presents with two stable solutions. There is one at low amplitude and another at higher amplitude beyond the activation threshold. The latter solution begins to degrade the efficiency of the NES. This parasitic amplitude peak is the beginning of the appearance of what is called the detached resonance.

By increasing the load to  $F_e = 15$  N, the analytical results presented in Figure 13 show that the amplitude level of the detached resonance becomes more important and could make the absorber inefficient if the

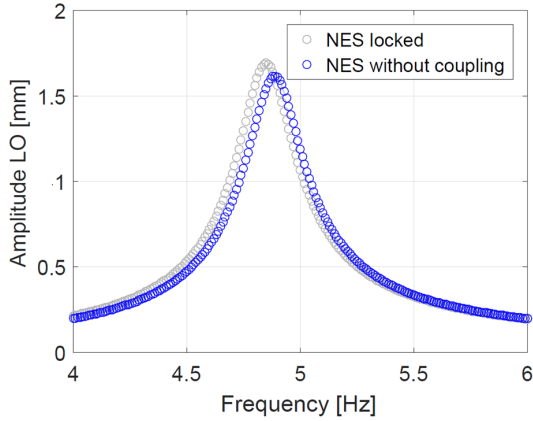


Figure 11: Evolution of the LO amplitude as a function of the frequency for  $F_e = 5$  N

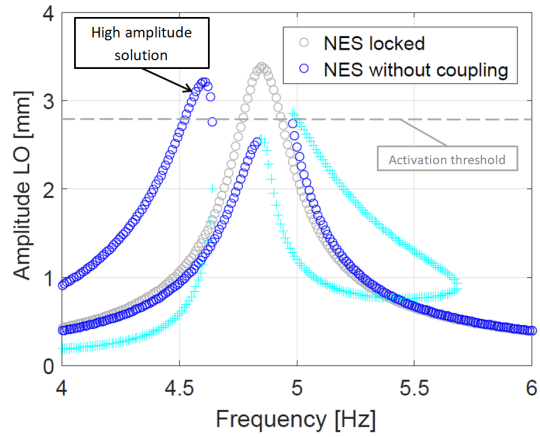


Figure 12: Evolution of the LO amplitude as a function of the frequency for  $F_e = 10$  N (o blue: stable solution; + turquoise: unstable solution)

structure passed over this branch of stable solutions while undergoing a disturbance which would cause it to jump onto the latter. Finally with a load  $F_e = 20$  N, Figure 14, in the area with multiple stable solutions, the solutions with low amplitudes "separate" towards the lower frequencies, leaving at 4.7 Hz the solution with high amplitude as the only possible solution. There is a fall to lower frequencies only for low amplitude solutions. As a result, the NES becomes inefficient.

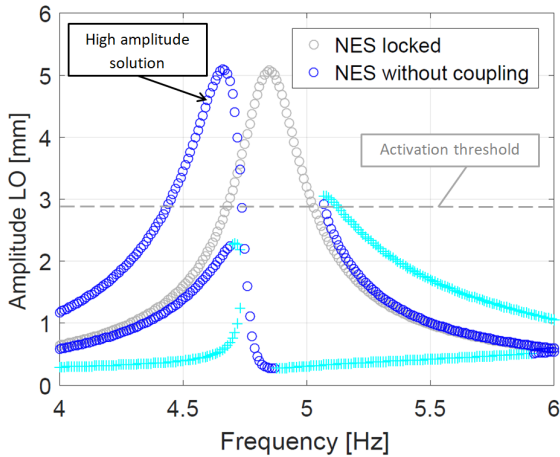


Figure 13: Evolution of the LO amplitude as a function of the frequency for  $F_e = 15$  N (o blue: stable solution; + turquoise: unstable solution)

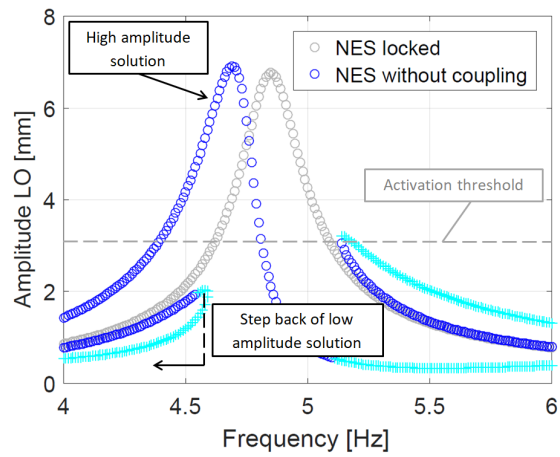


Figure 14: Evolution of the LO amplitude as a function of the frequency for  $F_e = 20$  N (o blue: stable solution; + turquoise: unstable solution)

This study of the absorber without the coil/magnet assembly shows its weaknesses. As soon as the forcing efforts allow the LO to reach the activation level, the risk of the appearance of a detached resonance is present, which can quickly cause the NES to lose its mitigation properties. This is mainly due to the low value of the damping coefficient of the absorber. By increasing its value, it would be possible to delay or even prevent the appearance of this parasitic amplitude peak as shown in Figure 15 where the analytical

calculation at  $F_e = 20$  N was done with a damping coefficient of the NES of  $c_2 = 12$  N/m.s<sup>-1</sup> instead of  $c_2 = 1$  N/m.s<sup>-1</sup> to compare with the Figure 14. This time, a desired solution is shown, the amplitude level of the structure remains below the activation threshold which has slightly increased from 2.8 mm to 3.3 mm and which corresponds to the value found by the SIM of Figure 10. The addition of the multiphysics coupling would make it possible to get this desired result by creating an electrical damping which would increase the equivalent damping of the absorber.

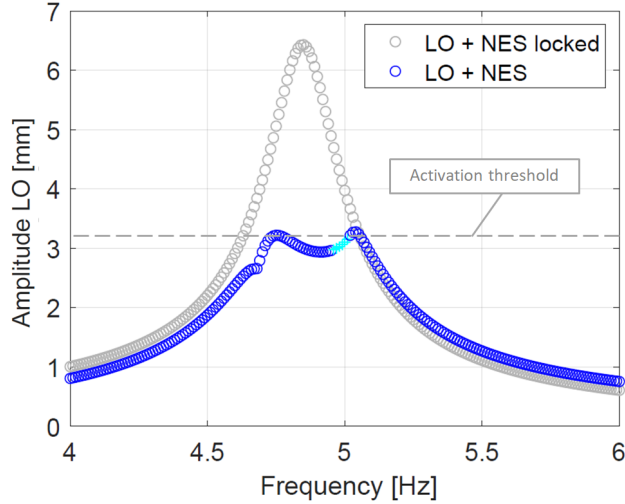


Figure 15: Evolution of the LO amplitude as a function of the frequency for  $F_e = 20$  N (o blue: stable solution; + turquoise: unstable solution) with a damping coefficient of the NES  $c_2 = 12$  N/m.s<sup>-1</sup>

#### 4.2. Experimental results

To highlight the potential of multiphysics coupling, experimental tests on our prototype is made and compared to the analytical model. During these tests, two configurations are studied for the multiphysics coupling. First of all, the electrical circuit is in the open position, the electrical resistance is infinite ( $R_{inf}$ ) and therefore the damping generated by the coil/magnet assembly is zero. Then, the circuit is in closed position, the resistance is minimum ( $R_{min}$ ) (internal resistance into the coil) and then the generated damping is maximum.

First of all, the results with the configuration of the NES without multi-physics coupling ( $R_{inf}$ ) are presented in Figure 16. The left figure shows the analytical results and the right figure shows the experimental results. First, for the configuration where the NES is blocked, the analytical and experimental results show a very close response with a maximum amplitude of 8 mm in both cases. For the NES configuration with ( $R_{inf}$ ), the experimental results show two different responses depending on whether one is sweep up or down. For sweep down, the LO shows a peak at high amplitude towards frequencies lower than  $f_0$ , making the NES inefficient. For sweep up, the attenuation of the vibratory level is well attenuated, going from 8 to 4 mm. A peak at higher amplitude begins to appear around the same frequency as that present in decreasing sine. These observations are in clear agreement with the analytical results obtained. The high amplitude peak is also present. However, despite the two possible stable solutions between 4 and 4.4 Hz in the analytical model, the high amplitude peak is a single possible solution for the LO. However, during the tests, this peak is not obtained for the sine sweep down, only a beginning of appearance is visible. This fact can be explained by the fact that our tests are sine sweeps, not allowing time for the system to stabilize on



the high amplitude solution which can take a few seconds.

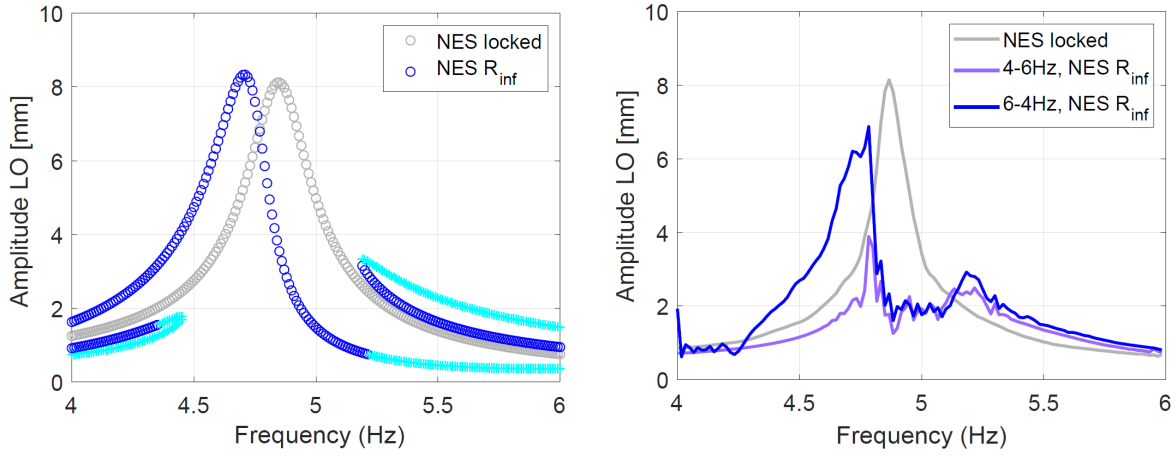


Figure 16: Evolution of the LO amplitude as a function of the frequency for  $F_e = 25$  N. The figure on the left introduces the analytical results (o blue: stable solution; + turquoise: unstable solution). The figure on the right introduces the experimental results

Now, the configuration with the maximum coupling ( $R_{min}$ ) is analyzed in Figure 17. In this case the analytical results are also coherent and close to the experimental results. For sine sweep up and down, the same responses are obtained and the model shows only one possible path. In both cases the attenuation of the vibratory level is similar, going from 8 mm to 3.7 mm during the tests and 3.8 mm for the model. Now, comparing Figure 16 and Figure 17, the influence of coupling is clear. As the NES "saturates" and becomes inefficient without coupling, it becomes satisfactory when the multiphysics coupling is added in order to increase its damping. This clearly shows the interest of having a calibrated damping. The difficulty in controlling the damping of a mechanical assembly here shows the limit of a purely mechanical NES.

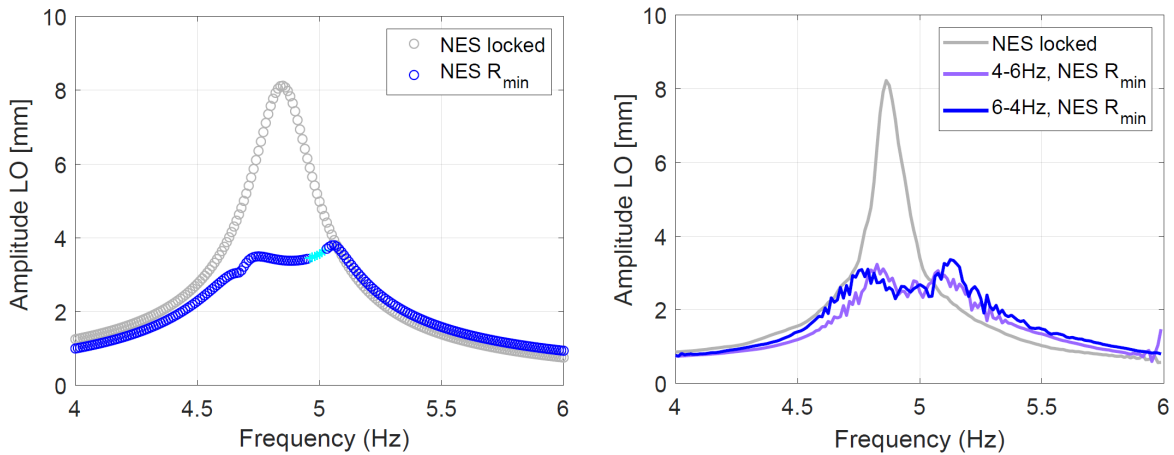


Figure 17: Evolution of the LO amplitude without and with NES +  $R_{inf}$  as a function of the frequency for  $F_e = 25$  N. The figure on the left introduces the analytical results (o blue: stable solution; + turquoise: unstable solution). The figure on the right introduces the experimental results

Its interest is also shown for a solicitation  $F_e = 30$  N. However, the amplitude level of the LO when the NES is blocked is higher during the tests compared to the analytical results. This is due to the fact that the limit of stroke of the LO springs is reached, causing shocks between the spirals and causing instabilities. The results in configuration without coupling ( $R_{inf}$ ) are shown in Figure 18. During the tests, whether for sweep up and down, the high amplitude peak is present. That is coherent with the analytical model since only one stable solution is present for a given frequency and also shows this peak. The discontinuity of stable solutions causing an amplitude jump to 5.3 Hz is also present in the experimental results.

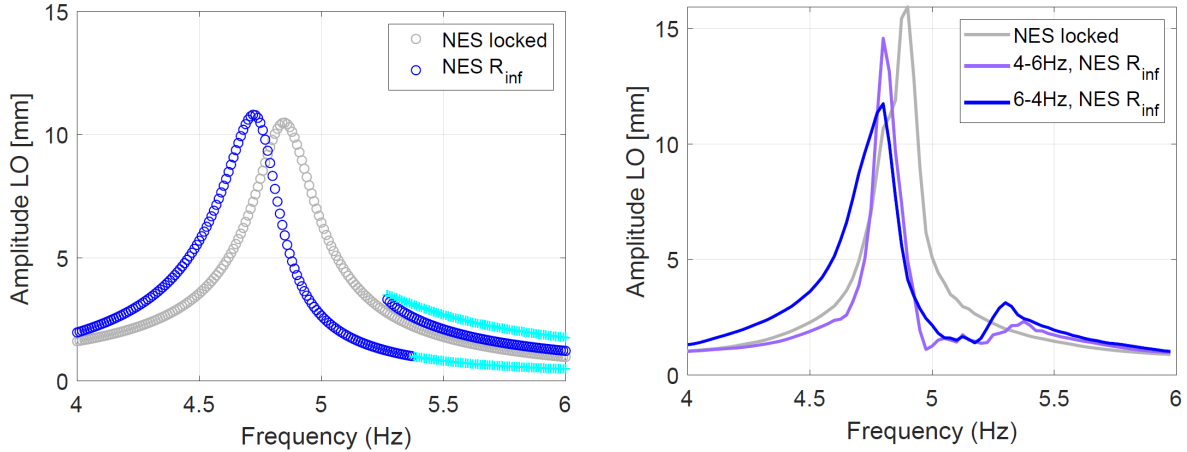


Figure 18: Evolution of the LO amplitude without and with NES +  $R_{inf}$  as a function of the frequency for  $F_e = 30$  N. The figure on the left introduces the analytical results (o blue: stable solution; + turquoise: unstable solution). The figure on the right introduces the experimental results

Finally, the results with the coupling activated are presented in Figure 19. While with zero multi-physics coupling, the NES still remained inefficient, the absorber still attenuates effectively with active coupling. Only the beginning of the appearance of a peak at higher amplitude appears at 4.7 Hz, whether in the analytical model or in experimental tests. While it represents a unique solution in the model, for sweep up, the LO does not present the start of a peak and its amplitude always remains well attenuated.

## 5. Conclusion

In this paper, the crucial role of the damping coefficient of a NES is emphasized. In fact, the analytical model shows that the NES efficiency is sensitive to its parameters and the model shows also the need to identify the set of parameters in order to avoid and to prevent the detached resonance. However, a purely mechanical nonlinear absorber has two shortcomings : the damping coefficient is difficult to control due to manufacturing tolerances or wear, and cannot be changed if desired. The method presented here to adapt the damping coefficient is the addition of an electro-magnetomechanical coupling to our system by the coil-magnet interaction. This coupling made it possible to create a damping of an electrical nature in addition to the mechanical damping allowing the increase of the equivalent damping of the absorber. The experimental tests, as well as the analytical model have shown the efficiency of the coupling making the NES more efficient. Despite the problems encountered on our structure considered as the LO, the analytical model gives a coherent and satisfactory prediction of the dynamic behavior of the LO.

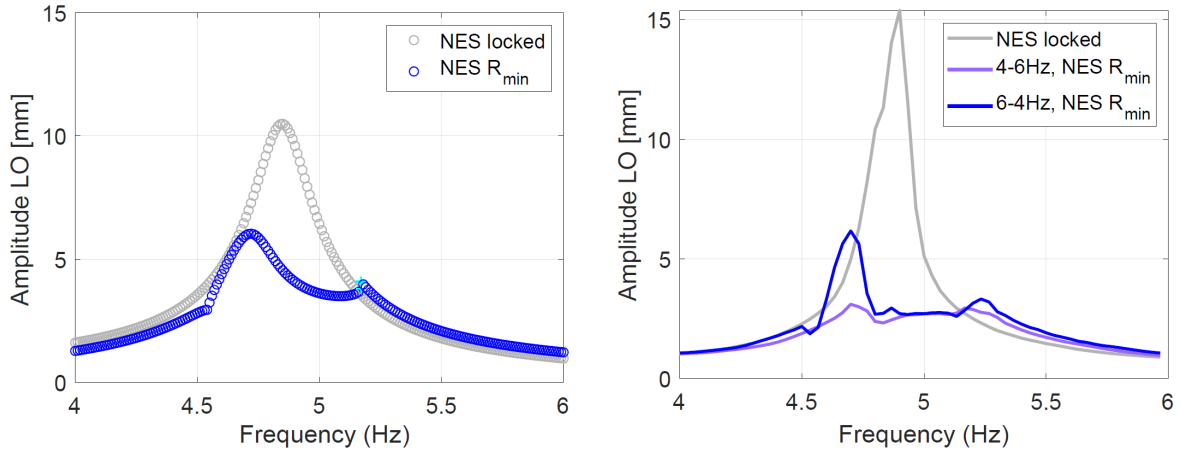


Figure 19: Evolution of the LO amplitude as a function of the frequency for  $F_e = 30$  N. The figure on the left introduces the analytical results (o blue: stable solution; + turquoise: unstable solution). The figure on the right introduces the experimental results

## 6. Acknowledgements

I would like to thank the French General Directorate of Armament (DGA) and the Defense Innovation Agency (AID) for its support and funding which made possible the realisation of its research work.

## References

- [1] R. Ibrahim. Recent advances in nonlinear passive vibration isolators. *Journal of Sound and Vibration*, 314:371–452, July 2008.
- [2] O. Gendelman. Transition of Energy to a Nonlinear Localized Mode in a Highly Asymmetric System of Two Oscillators. *Nonlinear Dynamics*, 25:237–253, January 2001.
- [3] A. F. Vakakis and O. Gendelman. Energy Pumping in Nonlinear Mechanical Oscillators: Part II—Resonance Capture. *Journal of Applied Mechanics*, 68(1):42–48, May 2000.
- [4] L. I. Manevitch, E. Gourdon, and C. H. Lamarque. Parameters optimization for energy pumping in strongly nonhomogeneous 2 dof system. *Chaos, Solitons & Fractals*, 31(4):900–911, February 2007.
- [5] G. Kerschen, Y. Lee, A. Vakakis, D. McFarland, and L. Bergman. Irreversible Passive Energy Transfer in Coupled Oscillators with Essential Nonlinearity. *SIAM Journal of Applied Mathematics*, 66:648–679, January 2005.
- [6] Y. Starosvetsky and O. V. Gendelman. Dynamics of a strongly nonlinear vibration absorber coupled to a harmonically excited two-degree-of-freedom system. *Journal of Sound and Vibration*, 312(1):234–256, April 2008.
- [7] Y. Starosvetsky and O. V. Gendelman. Strongly modulated response in forced 2DOF oscillatory system with essential mass and potential asymmetry. *Physica D: Nonlinear Phenomena*, 237(13):1719–1733, August 2008.
- [8] E. Gourc, G. Michon, S. Seguy, and A. Berlioz. Experimental Investigation and Design Optimization of Targeted Energy Transfer Under Periodic Forcing. *Journal of Vibration and Acoustics*, 136(2):021021–8, April 2014. Publisher: American Society of Mechanical Engineers.
- [9] G. Pennisi, C. Stephan, E. Gourc, and G. Michon. Experimental investigation and analytical description of a vibro-impact NES coupled to a single-degree-of-freedom linear oscillator harmonically forced. *Nonlinear Dynamics*, 88, May 2017.
- [10] Y. S. Lee, G. Kerschen, D. M. McFarland, W. J. Hill, C. Nickkawde, T. W. Strganac, L. A. Bergman, and A. F. Vakakis. Suppressing Aeroelastic Instability Using Broadband Passive Targeted Energy Transfers, Part 2: Experiments. *AIAA Journal*, 45(10):2391–2400, October 2007. Publisher: American Institute of Aeronautics and Astronautics.
- [11] Y. S. Lee, A. F. Vakakis, L. A. Bergman, D. M. McFarland, and G. Kerschen. Suppression Aeroelastic Instability Using Broadband Passive Targeted Energy Transfers, Part 1: Theory. *AIAA Journal*, 45(3):693–711, March 2007. Publisher: American Institute of Aeronautics and Astronautics.
- [12] S. Hubbard, R. Fontenot, D. McFarland, P. Cizmas, L. Bergman, T. Strganac, and A. Vakakis. Transonic Aeroelastic Instability Suppression for a Swept Wing by Targeted Energy Transfer. *Journal of Aircraft*, 51:1467–1482, September 2014.
- [13] E. Gourc, L. Dell’Elce, G. Kerschen, G. Michon, G. Aridon, and A. Hot. Performance Comparison Between a Nonlinear Energy Sink and a Linear Tuned Vibration Absorber for Broadband Control. *Nonlinear Dynamics*, 1:83–95, January 2016.
- [14] G. Pennisi, B. P. Mann, N. Naclerio, C. Stephan, and G. Michon. Design and experimental study of a Nonlinear Energy Sink coupled to an electromagnetic energy harvester. *Journal of Sound and Vibration*, 437:340–357, December 2018.

- [15] Z. H. Lai, G. Thomson, D. Yurchenko, D. V. Val, and E. Rodgers. On energy harvesting from a vibro-impact oscillator with dielectric membranes. *Mechanical Systems and Signal Processing*, 107:105–121, July 2018.
- [16] B. P. Mann and N. D. Sims. Energy harvesting from the nonlinear oscillations of magnetic levitation. *Journal of Sound and Vibration*, 319(1):515–530, January 2009.
- [17] A. Afsharfard. Application of nonlinear magnetic vibro-impact vibration suppressor and energy harvester. *Mechanical Systems and Signal Processing*, 98:371–381, January 2018.
- [18] Y. Jin, S. Hou, and T. Yang. Cascaded essential nonlinearities for enhanced vibration suppression and energy harvesting. *Nonlinear Dynamics*, 103(2):1427–1438, January 2021.
- [19] L. Manevitch. The Description of Localized Normal Modes in a Chain of Nonlinear Coupled Oscillators Using Complex Variables. *Nonlinear Dynamics*, 25:95–109, July 2001.
- [20] A. Sneller and B. Mann. On the nonlinear electromagnetic coupling between a coil and an oscillating magnet. *Journal of Physics D: Applied Physics*, 43:295005, July 2010.
- [21] G. Kerschen, J. Kowtko, D. McFarland, L. Bergman, and A. Vakakis. Theoretical and Experimental Study of Multimodal Targeted Energy Transfer in a System of Coupled Oscillators. *Nonlinear Dyn*, 47:285–309, January 2007.
- [22] E. Gourdon, N. A. Alexander, C. A. Taylor, C. H. Lamarque, and S. Pernot. Nonlinear energy pumping under transient forcing with strongly nonlinear coupling: Theoretical and experimental results. *Journal of Sound and Vibration*, 300(3):522–551, March 2007.